Inertia–Gravity Waves Generated within a Dipole Vortex

Chris Snyder

National Center for Atmospheric Research,* Boulder, Colorado

David J. Muraki

Department of Mathematics, Simon Fraser University, Vancouver, British Columbia, Canada

Riwal Plougonven

Laboratoire de Météorologie Dynamique, IPSL, Ecole Normale Supérieure, Paris, France

Fuqing Zhang

Department of Atmospheric Sciences, Texas A&M University, College Station, Texas

ABSTRACT

Vortex dipoles provide a simple representation of localized atmospheric jets. Numerical simulations of a synoptic-scale dipole in surface potential temperature are considered in a rotating, stratified fluid with approximately uniform potential vorticity. Following an initial period of adjustment, the dipole propagates along a slightly curved trajectory at a nearly steady rate and with a nearly fixed structure for more than 50 days. Downstream from the jet maximum, the flow also contains smaller-scale, upward-propagating inertia–gravity waves that are embedded within and stationary relative to the dipole. The waves form elongated bows along the leading edge of the dipole. Consistent with propagation in horizontal deformation and vertical shear, the waves' horizontal scale shrinks and the vertical slope varies as they approach the leading stagnation point in the dipole's flow. Because the waves persist for tens of days despite explicit dissipation in the numerical model that would otherwise damp the waves on a time scale of a few hours, they must be inherent features of the dipole itself, rather than remnants of imbalances in the initial conditions. The wave amplitude varies with the strength of the dipole, with waves becoming obvious once the maximum vertical vorticity in the dipole is roughly half the Coriolis parameter. Possible mechanisms for the wave generation are spontaneous wave emission and the instability of the underlying balanced dipole.

1. Introduction

Prominent inertia–gravity waves are often found beneath the downstream portion, or exit region, of localized upper-tropospheric jets (see the review by Uccellini and Koch 1987). Upward-propagating waves can also appear with a similar relation to the wind speed maximum, but in the stratosphere, above the tropospheric jet (e.g., Guest et al. 2000; Plougonven and Teitelbaum 2003). While the source of these observed waves is not yet settled, one possibility is that they arise spontaneously from the larger-scale jet. We examine that possibility in the present paper using numerical simulations of a dipole vortex in a rotating, stratified fluid. Because it possesses a localized jet between the two counter-rotating constituent vortices, the dipole vortex is a natural idealization of atmospheric "jet streaks" (Houghton et al. 1981; Van Tuyl and Young 1982; Cunningham and Keyser 2004).

Large-scale atmospheric and oceanic flows outside the Tropics are nearly balanced; that is, they can be described to a reasonable approximation by reduced equations sets, such as the quasigeostrophic (QG) equations, that filter inertia–gravity waves. In certain situations, however, inertia–gravity waves may arise spontaneously in an otherwise balanced flow. Examples

include fronts undergoing rapid frontogenesis (Snyder et al. 1993; Griffiths and Reeder 1996); elliptical vortices (Ford 1994a; Plougonven and Zeitlin 2002); idealized baroclinic waves (O'Sullivan and Dunkerton 1995; Zhang 2004; Plougonven and Snyder 2005, 2007); and rotating, stratified flows subjected to horizontal shear (Vanneste and Yavneh 2004). Fluid instabilities that couple balanced motions and inertia–gravity waves (Sakai 1989; Ford 1994b; Schecter and Montgomery 2003; Plougonven et al. 2005; Molemaker et al. 2005; Dritschel and Vanneste 2006) may also lead to the appearance of gravity waves in originally balanced flows. Though our intention is not to imply a single mechanism, for convenience we will use the term "wave generation" for all these instances in which balanced flows inherently produce inertia–gravity waves or are unstable to instabilities involving inertia–gravity waves.

Theory for inertia–gravity wave generation is most mature for rotating shallow-water flows having a Rossby number R of the order of one and a small Froude number (Ford et al. 2000). (Following typical notation, $R = U/fL$, where U is a horizontal velocity scale, L is a horizontal length scale, and f is the Coriolis parameter.) There is a direct mathematical analogy for this case to Lighthill's (1952) theory for the spontaneous emission of acoustic waves by vortical motion. The analysis proceeds by manipulating the governing equations into a single equation whose lhs is the linear operator for waves (acoustic or inertia–gravity, as the case may be) and whose rhs consists of terms of the form of two spatial derivatives acting on quadratic products of the dependent variables such as the components of velocity. Emitted waves in this case have spatial scales that are large compared to the characteristic scale of the balanced flow and phase speeds that are large compared to advective velocities.

Localized atmospheric jets (and our simulated vortex dipoles), on the other hand, are characterized by small R and are continuously stratified. These flows obey QG dynamics to a first approximation and have an aspect ratio H/L of the order of f/N, where N is the buoyancy frequency. The Froude number $F = U/NH$ is then also small, in contrast to the shallow-water theory for wave generation. When R is small, the time scales for inertia–gravity waves are much shorter than the advective time L/U that characterizes the balanced motion. Equivalently, for a stationary solution such as the dipole, $R \ll 1$ implies that the wavelengths of stationary inertia–gravity waves, which must be less than or comparable to $2\pi f/U$, are small relative to the length scale L of the dipole. We are interested in how waves appear in these otherwise balanced flow as R increases, but is still less than unity.

No general theory exists for fully stratified flows with small R, but both analytic examples and numerical simulations demonstrate that wave generation does occur. Vanneste and Yavneh (2004) show that plane-wave disturbances in sheared, rotating stratified flow generate inertia–gravity waves whose amplitude scales as $aR^{-1/2} \exp(-b/R)$, where a and b are known constants. Both Snyder et al. (1993) and Reeder and Griffiths (1996) present numerical simulations of wave generation by frontogenesis. They argue that wave generation at fronts follows from a mechanism, similar to that of Lighthill (1952), in which the balanced frontal circulation forces a gravity wave response that increases as the front contracts and the Lagrangian time scale for the frontogenesis decreases. Reeder and Griffiths have calculated the far-field wave response to the forcing and shown reasonable agreement with full simulations.

Our approach is to simulate numerically an idealized vortex dipole. The numerical solutions begin from the surface-trapped QG dipole for a uniform potential vorticity fluid of Muraki and Snyder (2007). This dipole is associated with a potential temperature anomaly on a flat horizontal boundary. In terms of atmospheric jet streaks, the rigid boundary may be thought of as a simple model for the tropopause and the computational domain can represent either the stratosphere above the jet streak or, inverting the vertical coordinate, the troposphere below the jet streak.

These initial conditions and the numerical model are described in section 2. We then present the numerical solution in section 3. After some transient adjustment associated with the initial conditions, the dipole begins to propagate nearly steadily and exhibits embedded, upward-propagating inertia–gravity waves of smaller scale that are stationary with respect to the dipole. To remove some residual oscillations and to rule out any association of those with the stationary inertia–gravity waves, we calculate (in section 4) time-averaged fields in a frame of reference moving with the dipole and then use them as initial conditions for additional simulations (in section 5). The stationary inertia–gravity waves are largely unaltered by this change of initial conditions. Section 6 analyzes the characteristics of the stationary waves, and section 7 presents the dependence of the waves on the Rossby number. Our results are summarized in section 8.

2. Preliminaries

a. Equations and the numerical model

As in previous idealized simulations of baroclinic waves (Snyder et al. 1991; Rotunno et al. 1994, 2000), we begin from the Boussinesq, f-plane primitive equa-

tions. Both nonhydrostatic and compressible terms are included, though they are negligible for the present simulations. The equations are summarized in Snyder et al. (1991).

The numerical techniques used in solving the equations of motion are also similar to those employed by Snyder et al. (1991), Rotunno et al. (1994), and Rotunno et al. (2000). The spatial discretization uses a C grid and centered fourth-order differences for the advective terms, while the temporal discretization is as in Klemp and Wilhelmson (1978) with a split-explicit scheme in which acoustic modes are integrated with a shorter time step that is implicit in the vertical. In addition, the numerical model includes damping of three-dimensional divergence, which further stabilizes the acoustic modes, and incorporates vertical advection of a reference profile of potential temperature on the small time step following Skamarock and Klemp (1992). An explicit, fourth-order horizontal diffusion is applied to the velocity and potential temperature with a coefficient of 0.01 times the ratio of the fourth power of the horizontal grid spacing to the time step.

The model has a domain of 3000 km in both horizontal directions and 15 km in the vertical. Vertical velocity is zero on the rigid upper and lower boundaries and the horizontal boundary conditions are periodic. The model includes a sponge layer above 12.5 km where the damping rate increases linearly from zero at the bottom of the layer to 10^{-4} s^{-1} at the model top.

For general aspects of the solution, we performed low-resolution runs, with 128 points in each horizontal direction and 64 points in the vertical, giving a grid spacing of 23.4 km horizontally and 250 m vertically. Runs with doubled horizontal and vertical resolution are used in the analysis of the inertia–gravity waves and to check for numerical artifacts.

b. Initial conditions

Initial conditions for the simulations are taken from the QG vortex dipole of Muraki and Snyder (2007). This dipole is a steadily propagating solution of the inviscid QG equations and is surface trapped, having uniform interior pseudopotential vorticity and a dipole in potential temperature on the lower boundary. Horizontal winds, pressure, and potential temperature are set to their geostrophic counterparts from the QG solution.

The QG dipole is determined solely by its nondimensional phase speed, which we take to be 1/9. The solution of Muraki and Snyder (2007) is then dimensionalized according to standard QG scaling using a horizontal length scale of $L = 500$ km, a horizontal velocity scale of $U = 10$ m s^{-1}, and values of $f = 10^{-4}$ s^{-1} for the

Coriolis parameter, $N = 10^{-2}$ s^{-1} for the Brunt–Väisälä frequency, and $\theta_0/g = 30.6$ K m^{-1} s^2 for the ratio of the reference potential temperature to the gravitational acceleration. The dimensional phase speed of the QG dipole is then roughly 1.1 m s^{-1}.

c. Estimating propagation speed

We estimate the dipole's propagation speed over a given time period by finding the translating reference frame in which the solution is most nearly steady. The time dependence is quantified by first time averaging the solution in the translating frame and then computing δ, the time average of the rms differences of the full solution from the time-averaged solution. We then seek the propagation speed $\mathbf{c}$ that minimizes δ by evaluating δ on a grid of values for $\mathbf{c}$ and refining that grid until the desired accuracy for $\mathbf{c}$ is achieved.

All propagation speeds given here are based on analysis of the two-dimensional field of potential temperature at the lowest model level. Other fields, such as low-level winds or vertical vorticity, give very similar propagation speeds.

Because of the initial adjustment of the dipole away from the QG dipole of Muraki and Snyder (2007), the potential temperature surrounding the dipole contains debris, which does not move with the dipole. This debris is excluded from the analysis of propagation speed by setting the differences from the time-averaged solution in a given frame to zero wherever their absolute value is less than 0.04 K.

3. Evolution from QG initial conditions

As discussed in section 2b, the initial conditions for the simulation are the geostrophic winds, potential temperature θ, and hydrostatic pressure from the QG dipole solution of Muraki and Snyder (2007). These initial conditions do not directly yield a steadily propagating solution of the primitive equations for two reasons.

First, because the initial conditions are purely geostrophic, the solution undergoes transient adjustment in which strong inertia–gravity waves radiate away from the dipole. These waves are clearly apparent in the vertical velocity w at early times as arcs of upward and downward motion expanding outward from the dipole (not shown). Consistent with this adjustment, time series of maximum and minimum w at a height of 5 km (Fig. 1) show large values and rapid variations at early times and then a decrease to much smaller values by 20 days.

Second, the full QG dipole (including ageostrophic winds) only approximates a steadily propagating solu-
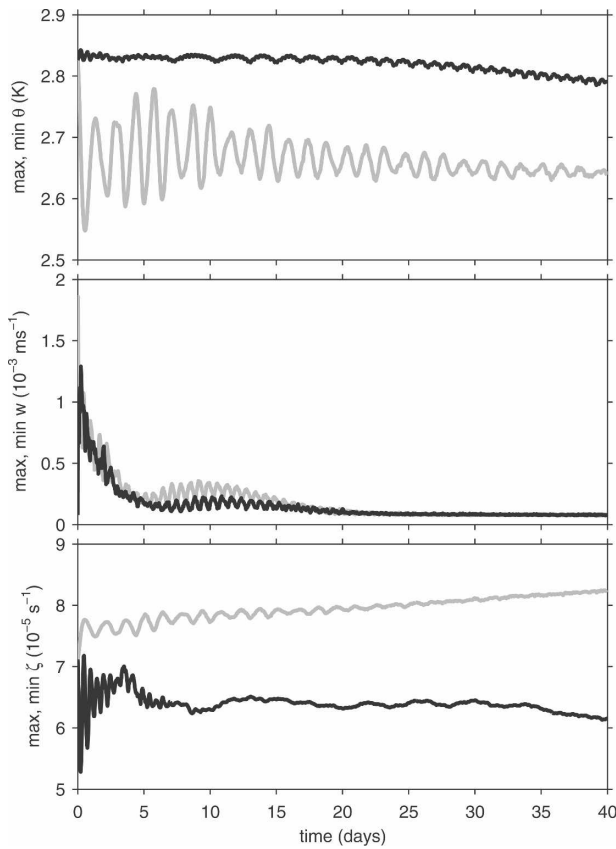
FIG. 1. Time series of maxima (black lines) and the negative of minima (gray) of (top) θ at the lowest model level, $z = 0.125$ km, (middle) w at $z = 5.25$ km, and (bottom) ζ at the lowest model level.

FIG. 2. Potential temperature θ at $z = 125$ m after $t = 12.5$, 25, and 37.5 days. Contour interval is 1/10 of the difference between the initial maximum and minimum of θ, or roughly 0.56 K, with positive and negative values shown in black and gray, respectively. Two periods of the domain are shown in x for clarity; in reality the dipole crosses the lateral boundary at $x = 3000$ km between days 12.5 and 25.

tion of the primitive equations. Thus, the dipole evolves away from the initially symmetric cyclone–anticyclone pair over the first few days. At the surface, the warm anomaly (associated with the cyclonic vortex) becomes elongated in the direction of propagation and shrinks in area, while the cold anomaly (associated with the anti-cyclone) becomes more circular and spreads in area (Fig. 2). Some of the warm air initially at the leading edge of the dipole passes southward around the anticy-clone and is ejected from the rear of the dipole.

Following the initial radiation of gravity waves and evolution of its structure, however, the dipole propa-gates with minimal further structural changes and along a curved path for the remainder of the 40-day simula-tion (Fig. 2). Thus, the dipole has returned to an ap-proximately steadily propagating solution, albeit with asymmetries between its cyclonic and anticyclonic sides and a curved, rather than linear, path. The latter be-havior resembles dipole solutions with a cyclonic "rider," which propagate in a large circle.

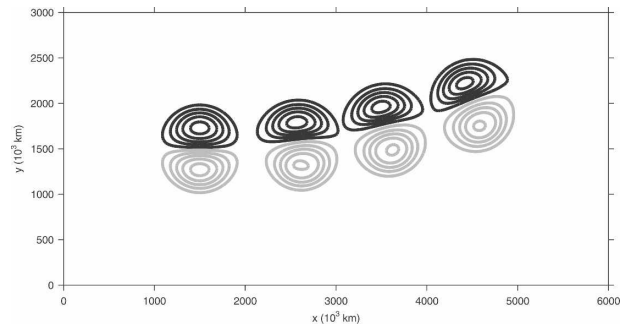The dipole also exhibits slower, secular trends in its

evolution. Time series of θ and the vertical vorticity ζ at the lowest model level, displayed in the bottom panel of Fig. 1, show a weakening of the warm anomaly and a steady, almost linear increase in the (magnitude of the) anticyclonic vorticity over 40 days. The minimum θ and the cyclonic ζ are both more variable but appear to have downward trends. While the model's weak fourth-order hyperdiffusion may account for the decrease of θ anomalies, the causes of the increase of ζ in the an-ticyclone are less obvious and are an open question for future work.

Figure 3 illustrates the structure of the dipole once it has returned to a nearly steadily propagating state. For θ, differences from the symmetric, QG solution are no-ticeable but not huge. The low-level w, however, has only a hint of the quadrupole of the QG solution, which has descent in the northeast and southwest quadrants and ascent to the southeast and northwest. Instead, w is organized into elongated bands, centered roughly on the dipole's central axis and with the amplitude increas-ing and the local wavelength decreasing toward the leading edge of the dipole (Fig. 3a). The bands are more prominent on the anticyclonic side of the dipole.

A vertical cross section along the central jet of the dipole reveals that the bands in w extend upward from the surface and tilt against the jet (i.e., to the east) with height (Fig. 3b). The pattern of w suggests an inertia–gravity wave and is consistent with upward group ve-locity. In sections 5 and 6, we will examine these bands in w in a higher-resolution simulation and present fur-ther evidence that they are in fact inertia–gravity waves.

As already noted, the dipole propagates almost steadily by this time. Animations of the fields shown in Fig. 3 indicate that the bands in the low-level vertical
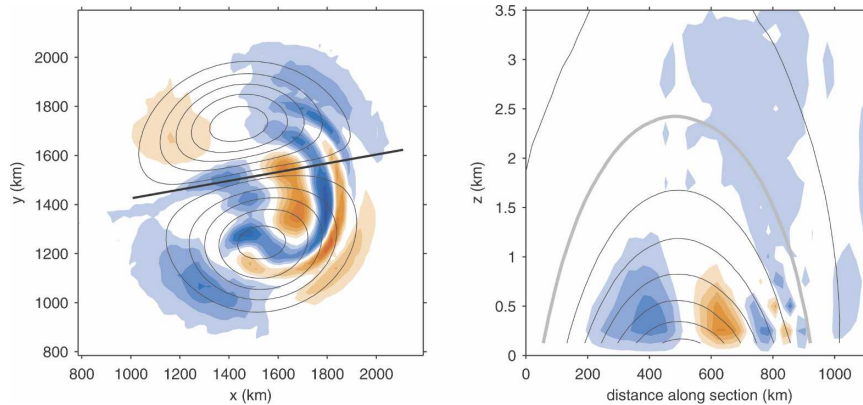
FIG. 3. The dipole at day 22. (left) Horizontal section of w at $z = 250$ m (colored, with red positive and blue negative) and θ at $z = 125$ m (thin black contours). (right) Vertical section along the thick line indicated in (a) of w (colored) and section-parallel horizontal velocity (black and gray contours). The contour interval for w in both panels is one-eighth the maximum value in the section of 0.8×10^{-3} m s^{-1} and that for the section-parallel velocity is 1 m s^{-1}. The potential temperature θ is shown as in Fig. 2. The gray contour in the right panel indicates where the section-parallel velocity is equal to 0.87 m s^{-1}, the propagation speed of the dipole.

velocity are, to a large extent, stationary with respect to the propagating dipole.

Time dependence remains, however, even in a frame of reference moving with the dipole. In addition to the slow decay of the dipole's signature in θ (Fig. 1), an elliptical distortion of θ that rotates anticyclonically with time is apparent within the low-level cold air. At higher levels (near $z = 5$ km), bands in w with wavelengths between 300 and 500 km propagate to the southwest. The amplitude of these bands is largest in an envelope centered to the southwest of the dipole and outside the dipole's horizontal perimeter as defined by surface θ. The next section gives a more detailed description of both these disturbances.

4. Time-averaged fields and deviations

Next we partition the dipole simulation between days 20 and 22 into a time-averaged component in the frame of reference moving with the dipole and deviations from that time average. This decomposition will substantiate our claims that the dipole is close to a steadily propagating solution and that the bands in the low-level vertical velocity seen in Fig. 3 are stationary with respect to the dipole. It also allows a clearer description of the remaining, time-dependent aspects of the simulation. Finally, in section 5, we will test whether the time dependence in these solutions is an inherent characteristic of the dipole or arises from the details of the initial conditions (through geostrophic adjustment or balanced remnants of the QG initial conditions).

The algorithm described in section 2c yields an esti-

mate of $\mathbf{c} = (0.86; 0.15)$ m s^{-1} for the propagation velocity between days 20 and 22. Since the dipole propagates neither precisely in a straight line nor precisely at constant speed, this value differs by up to 10% from estimates of $\mathbf{c}$ over 1-day intervals beginning between days 20 and 21. Some artifacts of the variations in the dipole's propagation will be apparent in the deviations from the time-averaged fields.

Time averages moving with the dipole are then calculated by integrating the governing equations in a frame of reference moving with velocity $\mathbf{c}$ and simply accumulating the average at each time step. Throughout the rest of the paper, we will work exclusively in this moving reference frame, where the dipole becomes a nearly steady solution.

We first consider w near the surface. Figure 4 shows a profile of $w(x)$ and its time average at the midpoint of the domain in y and $z = 250$ m. The banding in w is clearly evident and is well approximated by the time-averaged solution. Thus, the dipole's low-level w is nearly steady in this moving reference frame and the bands in w are, to a good approximation, stationary with respect to the dipole.

Figure 5 displays $\overline{\theta}$ and θ' at the lowest model level at day 21, where overbars and primes denote time-averaged fields and deviations from the time average, respectively. Throughout the 2-day period, the deviation field is no more than 3% of the amplitude of $\overline{\theta}$ and, as can be seen by comparing Figs. 2 and 5, $\overline{\theta}$ is close to the instantaneous θ. Again, the simulation is approximately steady in the frame moving with the dipole.

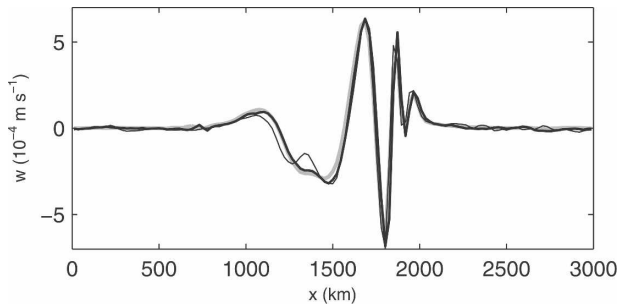The deviation field θ' at day 21 consists of a small-

FIG. 4. Vertical velocity as a function of x at $y = 1500$ km and $z = 250$ m. Values from Fig. 3a (i.e., from the original simulation at day 22) are shown with a thick black line, while $\overline{w}$, the time average between days 20 and 22 in the moving reference frame, is shown in gray. The thin black line indicates w from a 2-day simulation that uses time averages of all fields as initial conditions (see section 5). In some locations, the curves differ by so little that only the thick black line is visible.

scale couplet within the time-averaged anticyclone. Nearer the beginning and end of the averaging period, θ' also includes deviations with spatial scale comparable to the original dipole and amplitude comparable to that shown in Fig. 5 (not shown). This larger-scale component of θ' is associated with the variation of the dipole's propagation about the estimated velocity **c**.

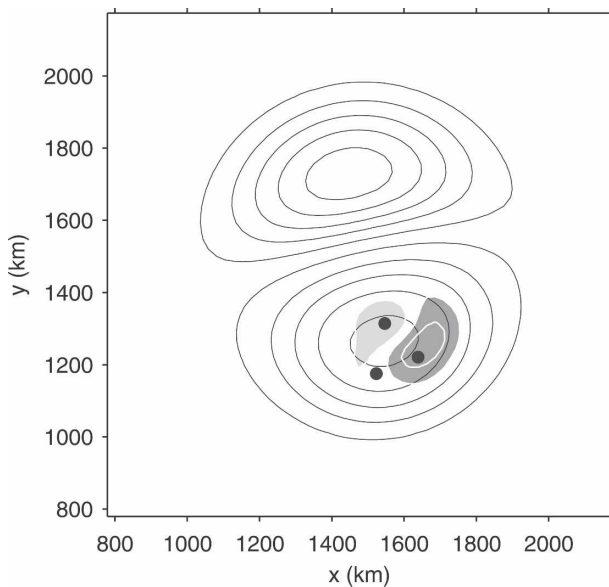The small-scale couplet, in contrast, rotates anticyclonically and with roughly constant amplitude about

FIG. 5. Potential temperature $\overline{\theta}$ (black contours) and θ' (white contours, with positive and negative values shaded light and dark gray, respectively) at $z = 125$ m and $t = 21$ days. Contours for $\overline{\theta}$ are the same as in Figs. 2 and 3, while those for θ' are shown at ± 0.01 K and every 0.02 K thereafter. Black dots indicate the locations of the time series in Fig. 7.
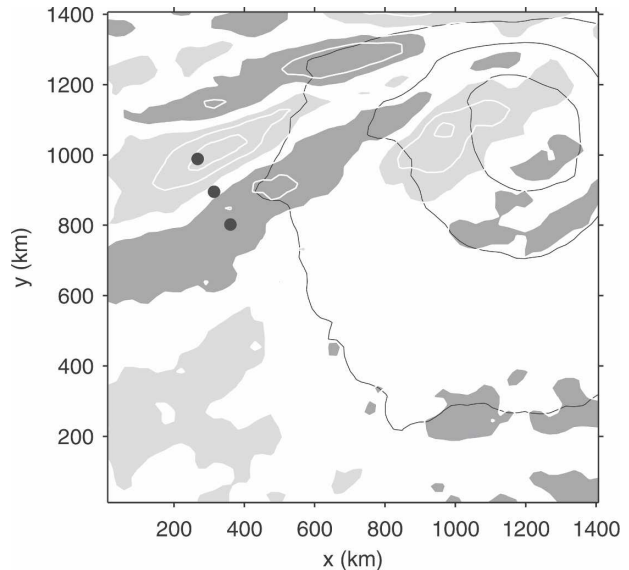

FIG. 6. Same as in Fig. 5, but for $\overline{w}$ and w' at $z = 5.25$ km and $t = 21$ days and for the southwestern quadrant of the dipole only. Contours for both fields are shown at $\pm 1 \times 10^{-5}$ m s^{-1} and every 2×10^{-5} m s^{-1} thereafter. Values of $\overline{w}$ are negative except along the upper edge of the figure. Black dots indicate the locations of the time series in Fig. 7.

the center of the time-averaged anticyclone, completing somewhat more than a full rotation over 2 days. The nature of this feature is not clear; it may be a near-inertial gravity wave trapped within the low absolute-vorticity fluid, or it may be a balanced wave propagating on the surface-θ gradient. We will show in section 5 that this feature depends on the detailed initial conditions chosen for the simulation and is not an inherent part of the dipole solution.

The horizontal structure of the time-dependent signal in w at midlevels is shown in Fig. 6. As already mentioned in section 3, the vertical velocity is organized into mesoscale bands. These bands are the dominant component of the deviations from $\overline{w}$ at this level. The time-averaged $\overline{w}$ is close to the synoptic-scale quadrupole that is expected from QG considerations to accompany the dipole. (Only one "quadrant" of $\overline{w}$ appears in Fig. 6, since only one-quarter of the domain is shown.)

The propagation of the mesoscale bands at 5.25 km, and of the couplet of θ' within the anticyclone, is illustrated by Fig. 7, which displays time series of θ' and w' at the locations of the black dots in Figs. 5 and 6. Both time series are roughly sinusoidal, with periods a little less than 2 days for θ' and a little less than 1 day for w'. Phase propagation, which can be inferred by the relation of time series at the three locations, is anticyclonic for θ' and southward for w'.
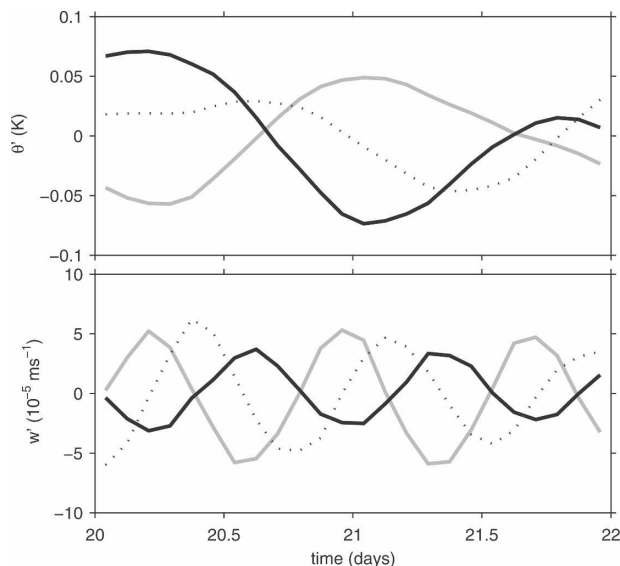
FIG. 7. Time series of (top) θ' at $z = 125$ m at the locations shown in Fig. 5 and (bottom) w' at $z = 5.25$ m at the locations shown in Fig. 6. Gray curves correspond to locations with positive values at day 21, black curves correspond to locations with negative values, and dotted curves correspond to "nodal" locations with values near zero.

5. Simulations initialized with time-averaged fields

Next we examine a simulation beginning from time-averaged fields, as in section 4, between days 20 and 22 and in a frame of reference moving with the dipole. This simulation tests the influence of the details of the initial conditions both on the stationary bands in w and on the time dependence that remains in the dipole.

The new simulation proceeds for two days, at which point we again perform time-averaging moving with the dipole over the 2 days. Figure 8 shows the time series of deviations of θ and w from the time average as in Fig. 7 (i.e., at the locations shown in Figs. 5 and 6). The time series begin at $t = 0$, the beginning of the new simulation, and continue for 2 days.

The different initial conditions for the new simulation greatly reduce the amplitude of the temporal oscillations seen in Fig. 7. The magnitude of the deviations from the time mean is also significantly reduced. Animations of θ and w at low levels confirm that the time dependence is greatly reduced relative to the original simulation. Nor do the temporal oscillations reappear in longer simulations (not shown). Thus, the oscillations identified in Figs. 5–7 are tied to the initial conditions for the simulation and are not directly associated with the dipole.

At the same time, the dipole and its associated bands in w are little changed between the two simulations.
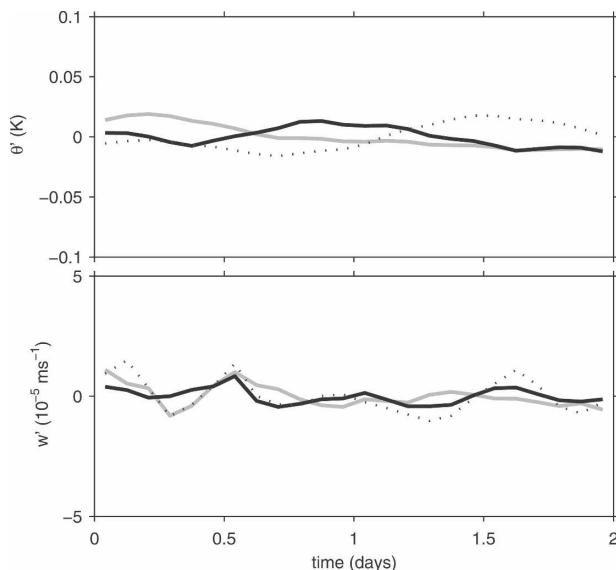

FIG. 8. Same as in Fig. 7, but for the simulation whose initial conditions are fields averaged in time between days 20 and 22.

Vertical velocities from the two simulations are compared in Fig. 4, which shows $w(x)$ for $y = 1500$ km, more or less along the central axis of the dipole, and $z = 250$ m. Though there are differences, the overall structure, amplitude, and phase of the waves agree well between the two simulations, demonstrating that the stationary bands (in contrast to the temporal oscillations) are robust to variations in the initial conditions.

Consistent with Fig. 4, horizontal and vertical sections of w at day 2 in the new simulation (not shown) are very similar to those from the previous simulation. The bands again extend in arcs along the dipole's leading edge, superposed on a weak signature of the QG quadrupole, and tilt toward the interior of the dipole with height.

We conclude that the stationary bands in w are inherent features of the dipole solution whose presence and structure are not sensitive to the initial conditions for the simulations. The time-dependent aspects of the simulations initialized from the QG dipole, on the other hand, appear to be related to the detailed initial conditions in that simulation. Since the waves shown in Fig. 3 are near the grid scale, especially in the vertical and near the dipole's leading edge, we have also investigated how they depend on the numerical resolution and the explicit dissipation included in the model.

a. Simulations with doubled resolution

In Fig. 9 and subsequent figures, we present results at day 22 from simulations using doubled resolution. The horizontal grid has 256^2 points and spacing of roughly
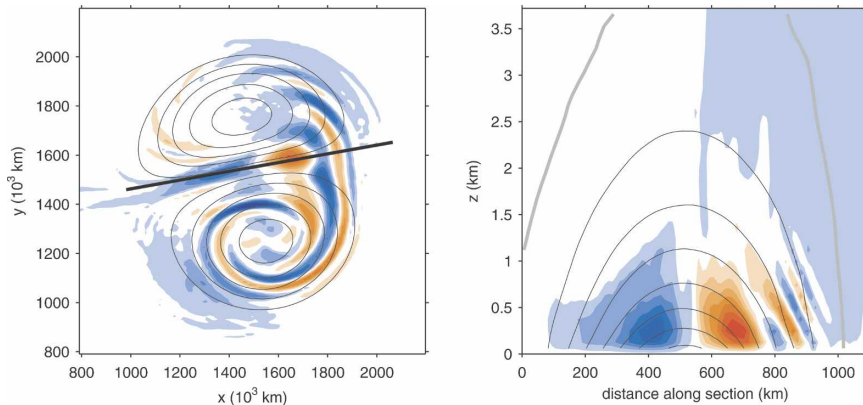
FIG. 9. Same as in Fig. 3, but for the simulation whose initial conditions are fields averaged in time between days 20 and 22 and that uses doubled resolution (horizontal grid spacing of 12 km). At this resolution, the lowest interior levels for θ and w shown in the left panel are at 62.5 and 125 m, respectively.

12 km, while the vertical grid has 128 levels and spacing of 125 m. The dimensional horizontal hyperdiffusion, which is tied to the spatial resolution and the time step, decreases by a factor of 8.

The evolution and overall structure of the dipole changes little in the higher-resolution simulation. The dipole still moves along a slightly curved path, although its propagation velocity $\mathbf{c} = (0.70, 0.15)$ m s^{-1} is somewhat slower than in the original simulation. The asymmetry between the warm and cold anomalies is also more pronounced.

The bands in this simulation are again stationary with respect to the dipole and have broadly similar spatial structure. The higher-resolution simulation produces larger-amplitude bands and yields additional detail in w, particularly along the outer edge of the warm, cyclonic vortex and within the cold anticyclone (cf. Figs. 9a and 3a). At the leading edge of the dipole, where the bands in the low-resolution simulation are almost at the grid scale, the high-resolution simulation clearly maintains the bands with larger amplitude and allows propagation farther aloft (Figs. 9b and 3b).

Away from the leading edge, however, the cross section along the dipole's axis reveals a very similar structure in the two simulations. Moving to the east along the section at low levels, both simulations have a broad region of descent centered near 400 km, followed by broad ascent near 700 km, then smaller-scale bands of descent and ascent near 800 and 850 km. Away from the leading edge, the bands are also reasonably well resolved in the high-resolution simulation, with horizontal and vertical wavelengths of around 100 km and 650 m, respectively.

Thus, while it is clear that the original simulations are not fully resolved, the low-level structure of the bands

away from the dipole's leading edge is not sensitive to a doubling of resolution. We conclude that the bands are not numerical artifacts. Moreover, the dependence on resolution of the bands near the leading edge is expected since, as will be described in the next section, they are inertia–gravity waves propagating in a deformation field and being strained to smaller scales by it.

b. Simulations with different dissipation

In addition to reducing the hyperdiffusion in the simulation with doubled resolution, we have also performed a number of experiments varying the magnitude and form of the dissipation with fixed, low resolution. Doubling or halving the fourth-order hyperdiffusion had effects similar to, but smaller than, those produced by doubling the resolution: the banding in w was still present, and with similar structure, but the bands' amplitude changed by roughly 25% (increasing if dissipation decreased; not shown). The most notable differences occurred in the anticyclone and near the stagnation point at the rear of the dipole, where additional weak bands appeared. (Qualitatively similar changes occur at doubled resolution; cf. Figs. 3 and 9.) When the hyperdiffusion decreased by a factor of 10, so that it was comparable to that used in the simulation with doubled resolution, the vertical velocity was dominated by noise of wavelength equal to twice the horizontal grid spacing. We also explored solutions using second-order diffusion. Using this less scale-selective dissipation led to the substantial decay of the dipole itself, so we took as initial conditions the fields at day 22 in the standard simulation (shown in Fig. 3) and integrated for only 4 days. The stationary bands were largely unchanged except for reduced amplitude (not shown). Thus, the presence and general structure of the

stationary bands does not depend sensitively on the dissipation, although their amplitude increases as the dissipation decreases.

6. Properties of the stationary inertia–gravity waves

We next analyze the properties of the bands in more detail. Figure 10 shows divergence, $-\partial w/\partial z$, in that portion of the cross section of Fig. 9b where the bands are most prominent. The cross section is approximately in the direction of the local wave vector for the bands.

First, consider how the horizontal and vertical wavelengths in the simulation compare with the dispersion relation for hydrostatic inertia–gravity waves. Looking in Fig. 10 near the location (880 km, 690 m), where the horizontal location is measured along the cross section, we estimate local horizontal and vertical wavelengths of 70 km and 520 m, respectively, with corresponding wavenumbers $k = 0.9 \times 10^{-4}$ m^{-1} and $m = 1.2 \times 10^{-2}$ m^{-1}. Averaging the Brunt–Väisälä frequency N and the dipole-relative flow U over a 70 km $\times$ 625 m box centered at the same (x, z) location, gives $N = 10^{-2}$ s^{-1} and $U = 1.2$ m s^{-1}.

The intrinsic frequency, $\tilde{\omega} = kU = 1.1 \times 10^{-4}$ s^{-2}, then compares well with the value 1.2×10^{-4} s^{-2} computed by substituting these values of k, U, and N into the dispersion relation:

$$\tilde{\omega}^2 = f^2 + N^2 k^2/m^2. \tag{1}$$

[Because the large-scale vertical velocity W scales as $R(H/L)U$, its contribution to $\tilde{\omega}$ is small and can safely be neglected. Moreover, the plane of the cross section lies more or less along the dipole's axis, where W is particularly small.] Comparisons at other locations with divergence of significant amplitude show similar agreement. Since the bands' structure is consistent with the dispersion relation for inertia–gravity waves, we will refer to them as gravity waves or simply waves in what follows.

The waves have the form of a packet extending upward from the surface and downstream (i.e., from left to right in Fig. 10, in the direction of the dipole-relative flow). The tilt of the phase lines is such that an observer moving with the flow will see downward phase propagation and hence the packet has upward group velocity. Figure 10 indicates the wave packet propagates upward 1.2 km over a horizontal distance of some 250 km, or at a slope of roughly 1/200. Using the estimated values of k, m, and N in the formulas for group velocity [obtained by taking derivatives w.r.t. k or m of (1)] gives the vertical propagation of the packet at roughly 0.4×10^{-2} m s^{-1} and the horizontal propagation upstream relative to the flow at 0.5 m s^{-1}. Since flow speeds are 1–2 m s^{-1}
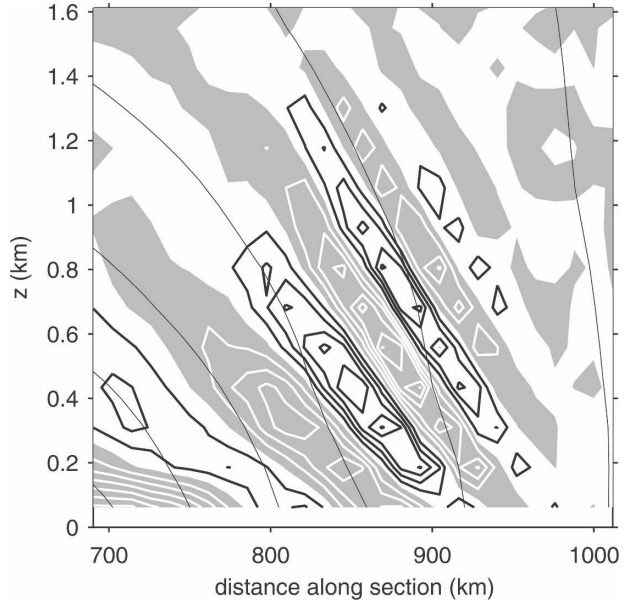

FIG. 10. Divergence (thick contours, negative values shaded) in the plane of the vertical cross section indicated in Fig. 9a, together with the section-parallel horizontal velocity (thin contours). Contour intervals are 10^{-3} s^{-1} for divergence and 1 m s^{-1} for velocity. Only a portion of the cross section indicated in Fig. 9a is shown.

near the center of the packet, this implies a downstream group propagation relative to the dipole at a slope of between 1/300 and 1/120, broadly consistent with what is shown in Fig. 10.

The horizontal and vertical variation of the dipole's flow also influences the structure of the waves. Near the wave packet, both the flow and the wave vector are nearly parallel to the section shown in Fig. 10; the variation of the flow normal to the section is also small. If we choose a coordinate system whose x axis is aligned with the section, the flow can be approximated locally as $u(x, z) = u_0 + \alpha x + \gamma z$. Assuming also that the waves are linear and $u(x, z)$ varies slowly on the wave scale, the local wavenumbers for the packet evolve according to (Jones 1969; Bühler and McIntyre 2005)

$$\frac{dk}{dt} = -\alpha k, \quad \frac{dm}{dt} = -\gamma k, \tag{2}$$

where the time derivatives are taken along ray paths (i.e., moving with the local group velocity). In Fig. 10, the flow is confluent ($\alpha < 0$) and decreases upward ($\gamma < 0$). Equation (2) predicts that both the horizontal and, after sufficient time, vertical wavenumbers increase exponentially at rate $-\alpha$ following the packet. Consistent with this prediction, local horizontal and vertical wavelengths estimated from Fig. 10 vary from 100 km and 650 m, respectively, at the location (840 km, 560 m), through 70 km and 520 m at (880 km, 690 m),

to less than 60 km and 500 m at (910 km, 810 m). Bühler and McIntyre (2005) argue that even in more complex flows wavenumbers will typically increase following a wave packet and note that, because the group velocity of inertia–gravity waves decreases with wavenumber, the packet will also begin to move with the local flow, a process they term "wave capture."

Figure 10 also shows that the slope of the phase lines steadily increases moving with the packet (upward and to the right). Given (2), the slope of the phase lines, k/m, evolves according to

$$\frac{d}{dt}(k/m) = (-\alpha + \gamma k/m)k/m. \tag{3}$$

The slope of phase lines will increase following the packet when $k/m < \alpha/\gamma$, that is, when that slope is less than the slope of lines of constant $u(x, z)$, which is given by α/γ. This is the situation shown in Fig. 10.

If the packet is subject to constant deformation and shear for sufficient time, the slope of phase lines approach the equilibrium slope, $k/m = \alpha/\gamma$. In this limit, the phase lines are parallel to the lines of constant u. Plougonven and Snyder (2005) found good agreement between α/γ and the slope of stratospheric inertia–gravity waves generated within a baroclinic wave. While there is some evidence of this alignment along the upper portion of the wave packet, the wave slope in the present simulation's slope does not approach α/γ closely over much of the packet, since the time scale for changes in k/m ($\alpha^{-1} \sim 10^5$ s) is comparable to the time required for the packet to traverse the region of significant vertical shear at a vertical group velocity of 0.5×10^{-2} m s^{-1} computed at the estimated k and m.

Finally, the model's fourth-order hyperdiffusion also has nonnegligible effects on the waves. The nondimensional coefficient for the hyperdiffusion is fixed at 1/100, giving a dimensional coefficient of $\nu = \Delta x^4/(100\Delta t)$, where Δx and Δt are the grid spacing and time step, respectively. At the extreme upper, eastern end of the packet, wavelengths are roughly $5\Delta x$, which implies a decay time $(\nu k^4)^{-1}$ of about 3.6×10^4 s or 10 h. Closer to the surface, however, the waves are better resolved and decay times are greater than 10^5 s owing to the scale selectivity of the hyperdiffusion.

7. Dependence on Rossby number

We next examine how the structure and magnitude of w in the solutions varies with the strength of the dipole. Varying the velocity scale U of the initial dipole while fixing the parameters f, N, and L of section 2b effectively varies the Rossby number, $R = U/fL$, of the experiment. All simulations in this section use the

coarser 23.4-km horizontal resolution (and 250-m vertical resolution).

When the dipole is weak and R is small, the QG dipole of Muraki and Snyder (2007) will approximate the full evolution closely. Varying R does not change the structure or evolution of the QG dipole; it simply changes the magnitude of the geostrophic velocities, which scale as R, and the time scale for evolution, which varies as R^{-1}. (In addition, the ageostrophic velocities, which are diagnostic in quasigeostrophy, scale as R relative to the geostrophic velocities or R^2 overall.) To facilitate comparison between simulations with different initial U, we extend each simulation having $U < 10$ m s^{-1} to a time equivalent under the QG scaling to the 22 days used when $U = 10$ m s^{-1}. For example, the simulation with $U = 1.25$ m s^{-1} covers 88 days. Simulations with $U \geq 10$ m s^{-1} all end at day 22 to minimize remnants of the initial adjustment, whose time scale is set by f^{-1} rather than U/L. Since w becomes quite small as U decreases, the simulations employ double-precision arithmetic when $U < 10$ m s^{-1}.

Figure 11 (top panels) displays w and θ on the lowest model levels above the surface at the end of five simulations with initial U ranging from 1.25 to 15 m s^{-1}. The domain in each panel is centered on the dipole, and contour values are normalized by the maximum w to emphasize the spatial structure of the fields; we will discuss how the magnitude of w varies with R later.

For $U = 1.25$ m s^{-1}, the vertical velocity is dominated by a large-scale quadrupole. In the center of the dipole along the jet axis, there is also a weak couplet of descent and ascent. A simulation with $U = 2.5$ m s^{-1} (not shown) is similar but has a stronger couplet relative to the quadrupole. At the other extreme ($U = 15$ m s^{-1}), inertia–gravity waves dominate the low-level vertical velocity. These waves are qualitatively similar to those in Figs. 3 and 9. They are, however, significantly stronger relative to the quadrupole and, as expected for near-inertial waves (Kunze 1985), more biased toward the anticyclone and its decreased absolute vorticity. With their increased amplitude, waves are also apparent along the northern edge of the cyclone up to the stagnation point at the rear of the dipole.

The transition between these two distinct structures for w occurs for U in the range of 5–10 m s^{-1}. At $U = 5$ m s^{-1}, the descent–ascent couplet along the jet axis becomes a prominent feature. At $U = 7.5$ m s^{-1}, the couplet continues to strengthen and waves are clearly apparent downstream. By $U = 10$ m s^{-1}, the case we have considered throughout the rest of the paper, the couplet and waves have larger amplitude than the quadrupole. As a reference for the value of R at which
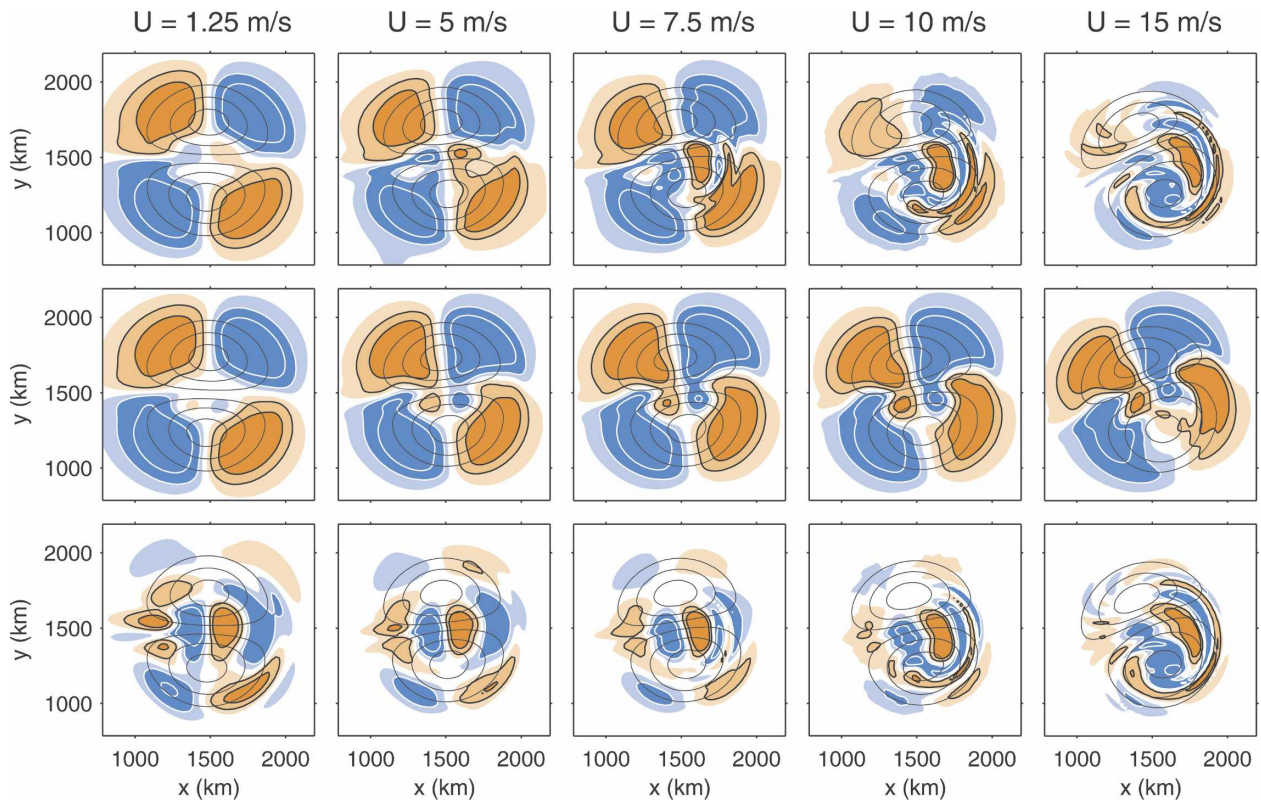
FIG. 11. Potential temperature θ overlaying (top) w, (middle) w_{QG}, and (bottom) $w - w_{QG}$ at the lowest interior levels for simulations with initial dipoles using $U = 1.25$, 5, 7.5, 10, and 15 m s^{-1}. Vertical velocity is contoured at $\pm 1/16$, $\pm 3/16$, and $\pm 7/16$ of its maximum value in each panel. White contours and blue shading indicate descent ($w < 0$). Only absolute values greater than $\pm 1/16$ are shaded. Thin lines are contours of θ as in Fig. 2. In each panel the plotting domain is centered on the dipole.

the waves appear, $U = 7.5$ m s^{-1} corresponds[1] to $R = U/fL = 0.15$.

The changes in θ across the entire range of U are much less dramatic. As U increases, the orientation of the dipole changes owing to its propagation along an increasingly curved trajectory (not shown). Asymmetries between the cyclone and anticyclone also develop at larger U, with the anticyclone becoming more circular and the cyclone less so.

A quadrupole in w arises at the level of the QG approximation.[2] To reveal more precisely how w differs

from that predicted by QG theory, we have computed w_{QG}, the QG vertical velocity, given θ and the geostrophic velocities $\mathbf{v}_g$ from each simulation. Solving

$$\left[N^2 \left(\frac{\partial^2}{\partial x^2} + \frac{\partial^2}{\partial y^2} \right) + f^2 \frac{\partial^2}{\partial z^2} \right] w_{QG} = 2\nabla \cdot \mathbf{Q}, \quad (4)$$

where $\mathbf{Q} = -g/\theta_0(\partial \mathbf{v}_g/\partial x \cdot \nabla\theta, \partial\mathbf{v}_g/\partial y \cdot \nabla\theta)$, yields w_{QG} (Gill 1982, his section 12.10).

Results for w_{QG} are shown in the middle panels of Fig. 11. As expected, a quadrupole with scale comparable to the vortex dipole itself is the strongest signal across all the experiments. Near the center of the dipole, however, there are additional features; these strengthen relative to the larger-scale quadrupole as R increases and have the form of an ascent–descent couplet along the dipole's axis. We have not developed a comprehensive explanation for these features in the

[1] The precise value of R of course depends on the definition chosen. Using the maximum wind speed in this simulation (6 m s^{-1}) and the distance between extrema in the ascent–descent couplet (250 km), which gives a Rossby number of 0.24. A Rossby number based on the maximum vertical vorticity would be even larger since relative vorticity in the anticyclone reaches $-0.6\,f$ at this time.

[2] Northward ageostrophic flow near the surface at the upstream end of the geostrophic jet accelerates parcels entering the jet and southward ageostrophic flow has the opposite effect in the downstream "exit region" of the jet. This leads to a thermally direct

circulation upstream with descent on the colder, southern side of the jet axis and ascent to the north, and the opposite pattern of w downstream of the jet.

center of the dipole, but detailed examination of the various terms contributing to $\nabla \cdot \mathbf{Q}$ indicates large sensitivity to the slight bowing of the cold anomaly across the dipole's axis, which increases as R increases.

Of more interest is the difference between w and w_{QG}, displayed in the bottom panels of Fig. 11. The most prominent features are a pronounced descent–ascent couplet that is present for all R and, for U larger than 5 m s^{-1}, inertia–gravity waves downstream from the couplet. The descent–ascent couplet is more cleanly captured in $w - w_{QG}$—most of the complicated central structure in w appears to come from w_{QG}. Removing w_{QG} also makes the wave propagation along the cyclone's outer edge much more obvious.

Figure 12 quantifies the amplitude dependence of w, w_{QG}, and their difference on the maximum wind speed in the dipole. To the extent that the wave generation may be associated with the dipole's jet, the maximum wind speed is a natural surrogate for R, since the dipole's scale varies little across the simulations. (The maximum wind speed at the end of the simulations also varies nearly linearly with U and is approximately given by $0.85U$.) Lacking an obviously better choice, we measure w, w_{QG}, and $w - w_{QG}$ by their maximum values at $z = 250$ m.

The full w increases as a power of the wind speed (i.e., linearly in the log–log scale of Fig. 12) up to wind speeds of roughly 6 m s^{-1} (corresponding to $U = 7.5$ m s^{-1}) then begins a more rapid increase. This behavior hints at the emergence of a second dynamical process affecting w, consistent with the onset of wave generation shown in Fig. 11. For small wind speeds, w_{QG} is the dominant contribution to w but w_{QG} retains power-law behavior across the entire set of simulations. For large wind speeds, w is much larger than w_{QG}.

The exponents for $w - w_{QG}$ and w_{QG} provide information about the underlying dynamics. The slope of w_{QG} in Fig. 12 is 2.1, which conforms to the QG prediction that w scales as R^2 [as implied by the quadratic dependence of $\nabla \cdot \mathbf{Q}$ in (4) on the geostrophic flow]. In contrast, the best-fit line for the first three points of $w - w_{QG}$ has a slope of 3.1. This slope is consistent with next-order, $O(R^3)$ balanced corrections to w_{QG} that could be obtained by expanding the primitive equations in R as in, for example, Muraki et al. (1999). The ascent–descent couplet along the jet axis in both w and $w - w_{QG}$ thus arises as a balanced correction to QG theory.

For larger wind speeds, $w - w_{QG}$ exhibits an approximate R^4 dependence (a slope of 3.9). The transition to this steeper slope again coincides with the appearance of obvious waves in $w - w_{QG}$. While we believe the steeper slope is a reflection of wave generation, we
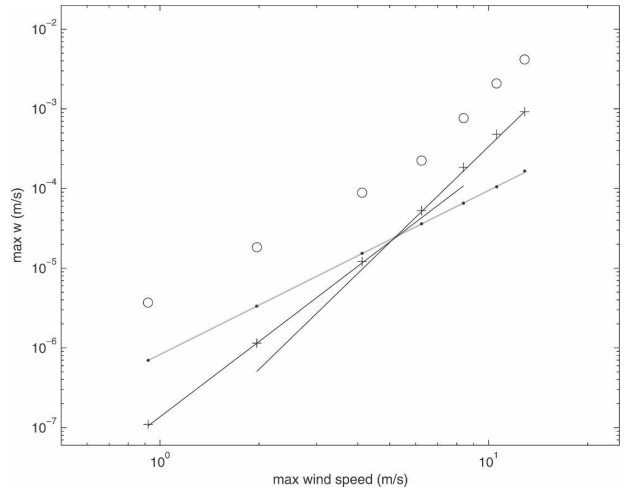

FIG. 12. Maximum absolute values of w at $z = 250$ m as a function of the maximum jet speed in the dipole (open circles). Data are shown for each of the simulations in Figs. 11 and 12, along with simulations using $U = 2.5$ and 12.5 m s^{-1}. Also shown are the maximum absolute values for w_{QG} (dots) and $w - w_{QG}$ (crosses) and best-fit lines for w_{QG} (gray) and the first three and last four points of $w - w_{QG}$ (thin lines). Those lines have slopes of 2.06, 3.14, and 3.88, respectively.

attach little significance to the R^4 dependence because of the presence in $w - w_{QG}$ of contributions other than waves. We have also tried to separate the waves from the rest of $w - w_{QG}$ by bandpass filtering all wavelengths greater than 1/10 of the domain size. This small-scale component of $w - w_{QG}$ increases significantly more rapidly with R, exhibiting a slope of 6 for 5 m s$^{-1} \leq U \leq 10$ m s^{-1}. A higher-order balanced approximation to w will be necessary if we wish to quantify more precisely the variation with R of the wave generation alone.

8. Summary and discussion

This paper has analyzed numerical simulations of a synoptic-scale vortex dipole in a rotating, stratified fluid. These simulations provide an example of the generation of inertia–gravity waves by balanced flows. Our choice of a dipole is motivated as an idealization of atmospheric "jet streaks," which are often associated with generation of inertia–gravity waves, and by its simple dynamics (approximately steady propagation).

Beginning with geostrophic initial conditions taken from the surface-trapped QG dipole of Muraki and Snyder (2007), the dipole undergoes a transient period in which waves radiate rapidly upward and away from the dipole and the symmetry of the QG solution is broken, with the anticyclone expanding and the cyclone shrinking. These transient waves arise through classical geostrophic adjustment (Blumen 1972) or its generali-

zations. Following the initial period of adjustment, the dipole propagates along a slightly curved trajectory at a nearly steady rate and with a nearly fixed structure for many tens of days.

For dipoles that are sufficiently intense, with a Rossby number R based on the jet speed and the dipole radius of $O(10^{-1})$ and maximum relative vorticity of roughly 0.5 f, the flow also contains smaller-scale, upward-propagating inertia–gravity waves that are embedded within and stationary relative to the dipole. The waves appear downstream from the jet maximum, forming elongated bows aligned with the leading edge of the dipole, and have strong similarities to the near-inertial waves in the stratosphere found in baroclinic wave simulations (O'Sullivan and Dunkerton 1995; Plougonven and Snyder 2005, 2007).

In addition to the stationary waves, there are weaker oscillations that appear to be long-lasting consequences of the initial adjustment. These oscillations can be largely removed by time averaging the solutions in a frame of reference moving with the dipole and then restarting the simulation from the time-averaged fields. The stationary waves are almost unaffected by this procedure.

The stationary waves persist throughout the 40-day (or longer) integrations despite the model's explicit horizontal hyperdiffusion, which on its own damps motions at the scale of the waves on much shorter time scales. This argues strongly that the waves are an inherent feature of sufficiently strong dipoles rather than remnants of the initial adjustment. The wave characteristics are also clearly modified by their propagation through horizontal deformation and vertical shear, much as predicted theoretically by Bühler and McIntyre (2005) and demonstrated in baroclinic wave life cycles by Plougonven and Snyder (2005): their horizontal scale shrinks and the vertical slope varies as wave packets approach the leading stagnation point in the dipole's flow.

We have also explored the dependence of the wave generation on R by varying the amplitude of the initial QG dipole over an order of magnitude. For dipoles of radius 500 km, stationary inertia–gravity waves obviously first appear once the maximum jet speed reaches roughly 6 m s^{-1}. To examine the waves' amplitude and structure more precisely, we have calculated the QG vertical velocity w_{QG} based on the simulated pressure field and subtracted this contribution from the full w. When R is very small, the most prominent feature in $w - w_{QG}$ is a couplet of descent and ascent along the jet axis and centered on the jet maximum. Its amplitude increases approximately as R^3, indicating that it arises from next-order, balanced corrections to w_{QG}. For larger R, waves appear and $w - w_{QG}$ increases significantly more rapidly.

In the exit region of the jet where their amplitude is largest, the stationary waves' general structure has little dependence on the model resolution, or on the form or magnitude of model dissipation. The amplitude of the waves is more sensitive to dissipation, as is the detailed structure of the wave field, especially near the stagnation points at the leading and trailing edges of the dipole and within the anticyclone. Aside from the inertia–gravity waves, the numerical solutions are very well resolved. The dependence on resolution arises not through truncation errors but mainly because we decrease the model's hyperdiffusion as the resolution increases—the waves are strained to small scales in many regions of the flow and thus are sensitive to the model dissipation.

These dipole simulations add to the list of idealized examples in which balanced flows generate inertia–gravity waves spontaneously, including frontogenesis, vortices in shallow water and continuously stratified flow, baroclinic waves, sinusoidal disturbances in sheared rotating stratified flow, and instabilities that couple balanced motions and inertia–gravity waves. The dipole and its embedded waves, both of which are approximately steady in an appropriate frame of reference, differ from other examples in which time dependence of the balanced flow leads to wave emission (Ford 1994a; Vanneste and Yavneh 2004). Moreover, unlike the examples of Lighthill radiation (Ford 1994a; Plougonven and Zeitlin 2002), the dipole has a small Rossby number and the waves are on the small scale compared to the balanced motions. On the other hand, the waves in the dipole resemble those associated with upper-level jets in baroclinic wave simulations (Plougonven and Snyder 2005, 2007): they appear downstream of a localized jet and near a system-relative stagnation point, and they have arcing phase lines that are stationary with respect to the jet exit and roughly normal to the flow.

"Geostrophic adjustment" is one mechanism previously suggested for the generation of inertia–gravity waves within synoptic-scale flows (Uccellini and Koch 1987). This terminology seems inappropriate for the dipole since classical geostrophic adjustment is a transient process, dependent on initial conditions and occurring on a time scale of several inertial periods. In the dipole, the waves are not transient but steady over tens of days; they are not sensitive to initial conditions except to the extent that the dipole is; and if anything, the dipole itself appears to be intensifying by some measures rather than becoming more balanced (Fig. 1, bottom panel).

We advocate an alternative mechanism,[3] beginning from the apparently reasonable assumption that the dipole can be closely approximated by a balanced solution. Deviations from that balanced solution, if they are sufficiently small, will then satisfy linear equations given by linearizing the primitive equations about the balanced solution and forcing by the residual tendencies (i.e., the difference between the tendencies predicted by the balanced solution and those obtained upon substitution of the balanced fields into the full primitive equations). Unless the balanced solution is so simple that there is no projection onto temporal and spatial scales for which there are propagating inertia–gravity waves, the forcing inherently produces some wave response. This argument immediately predicts that a (nearly) steady balanced flow, such as the dipole, must generate steady inertia–gravity waves.

Because its balanced dynamics are steady and uncomplicated, the dipole is a particularly simple setting for further study of wave generation. A clear demonstration of the mechanism for the wave generation is an important next step. We expect that this will also require a more quantitative understanding of the wave propagation through the spatially varying flow of the dipole. Another direction for further study is the effect of the wave generation on the dipole's evolution.

We have not attempted to explain the secular increase in the maximum anticyclonic vorticity, but it is suggestive of back reaction on the dipole from the wave generation.

REFERENCES

Blumen, W., 1972: Geostrophic adjustment. *Rev. Geophys. Space Phys.,* **10,** 485–528.

Bühler, O., and M. E. McIntyre, 2005: Wave capture and wave–vortex duality. *J. Fluid Mech.,* **534,** 67–95.

Cunningham, P., and D. Keyser, 2004: Dynamics of jet streaks in a stratified quasi-geostrophic atmosphere: Steady-state representations. *Quart. J. Roy. Meteor. Soc.,* **130,** 1579–1609.

Dritschel, D. G., and J. Vanneste, 2006: Instability of a shallow-water potential-vorticity front. *J. Fluid Mech.,* **561,** 237–254.

Ford, R., 1994a: Gravity wave radiation from vortex trains in rotating shallow water. *J. Fluid Mech.,* **281,** 81–118.

——, 1994b: The instability of an axisymmetric vortex with monotonic potential vorticity in rotating shallow water. *J. Fluid Mech.,* **280,** 303–334.

——, 1994c: The response of a rotating ellipse of uniform potential vorticity to gravity wave radiation. *Phys. Fluids,* **6A,** 3694–3704.

——, M. E. McIntyre, and W. A. Norton, 2000: Balance and the slow quasimanifold: Some explicit results. *J. Atmos. Sci.,* **57,** 1236–1254.

Gill, A. E., 1982: *Atmosphere–Ocean Dynamics.* Academic Press, 662 pp.

Griffiths, M., and M. J. Reeder, 1996: Stratospheric inertia-gravity waves generated in a numerical model of frontogenesis. I: Model solutions. *Quart. J. Roy. Meteor. Soc.,* **122,** 1153–1174.

Guest, F., M. J. Reeder, C. J. Marks, and D. J. Karoly, 2000: Observations of stratospheric inertia-gravity waves over Macquarie Island. *J. Atmos. Sci.,* **57,** 737–752.

Houghton, D. D., W. H. Campbell, and N. D. Reynolds, 1981: Isolation of the gravity-inertial motion component in a nonlinear atmospheric model. *Mon. Wea. Rev.,* **109,** 2118–2130.

Jones, W. L., 1969: Ray tracing for internal gravity waves. *J. Geophys. Res.,* **74,** 2028–2033.

Klemp, J. B., and R. B. Wilhelmson, 1978: The simulation of three-dimensional convective storm dynamics. *J. Atmos. Sci.,* **35,** 1070–1096.

Kunze, E., 1985: Near-inertial wave propagation in geostrophic shear. *J. Phys. Oceanogr.,* **15,** 544–565.

Lighthill, M. J., 1952: On sound generated aerodynamically. I. General theory. *Proc. Roy. Soc. London,* **211A,** 564–587.

Molemaker, J. M., J. C. McWilliams, and I. Yavneh, 2005: Baroclinic instability and loss of balance. *J. Phys. Oceanogr.,* **35,** 1505–1517.

Muraki, D., and C. Snyder, 2007: Vortex dipoles for surface quasigeostrophic models. *J. Atmos. Sci.,* **64,** 2961–2967.

——, ——, and R. Rotunno, 1999: The next-order corrections to quasi-geostrophic theory. *J. Atmos. Sci.,* **56,** 1547–1560.

O'Sullivan, D., and T. J. Dunkerton, 1995: Generation of inertia-gravity waves in a simulated life cycle of baroclinic instability. *J. Atmos. Sci.,* **52,** 3695–3716.

Plougonven, R., and V. Zeitlin, 2002: Internal gravity wave emission from a pancake vortex: An example of wave-vortex interaction in strongly stratified flows. *Phys. Fluids,* **14,** 1259–1268.

——, and H. Teitelbaum, 2003: Comparison of a large-scale inertia-gravity wave as seen in the ECMWF analyses and from radiosondes. *Geophys. Res. Lett.,* **30,** 1954, doi:10.1029/2003GL017716.

——, and C. Snyder, 2005: Gravity waves excited by jets: Propagation versus generation. *Geophys. Res. Lett.,* **32,** L18802, doi:10.1029/2005GL023730.

——, and ——, 2007: Inertia–gravity waves spontaneously generated by jets and fronts. Part I: Different baroclinic life cycles. *J. Atmos. Sci.,* **64,** 2502–2520.

——, D. J. Muraki, and C. Snyder, 2005: A baroclinic instability that couples balanced motions and gravity waves. *J. Atmos. Sci.,* **62,** 1545–1559.

Reeder, M. J., and M. Griffiths, 1996: Stratospheric inertia-gravity waves generated in a numerical model of frontogenesis. II: Wave sources, generation mechanisms and momentum fluxes. *Quart. J. Roy. Meteor. Soc.,* **122,** 1175–1195.

Rotunno, R., W. C. Skamarock, and C. Snyder, 1994: An analysis of frontogenesis in numerical simulations of baroclinic waves. *J. Atmos. Sci.,* **51,** 3373–3398.

——, D. M. Muraki, and C. Snyder, 2000: Unstable baroclinic waves beyond quasi-geostrophic theory. *J. Atmos. Sci.,* **57,** 3285–3295.

---

[3] Reeder and Griffiths (1996) present numerical calculations that point to this mechanism for waves generated by frontogenesis. This mechanism is also related to the mathematically rigorous theory of Ford et al. (2000) for shallow water, though that theory explicitly considers only waves in the far field, away from a localized region of balanced flow.

Sakai, S., 1989: Rossby–Kelvin instability: A new type of ageo-strophic instability caused by a resonance between Rossby waves and gravity waves. *J. Fluid Mech.,* **202,** 149–176.

Schecter, D. A., and M. T. Montgomery, 2003: On the symmetri-zation rate of an intense geophysical vortex. *Dyn. Atmos. Oceans,* **37,** 55–88.

Skamarock, W. C., and J. B. Klemp, 1992: The stability of time-split numerical methods for the hydrostatic and nonhydro-static elastic equations. *Mon. Wea. Rev.,* **120,** 2109–2127.

Snyder, C., W. C. Skamarock, and R. Rotunno, 1991: A compari-son of primitive equation and semigeostrophic simulations of baroclinic waves. *J. Atmos. Sci.,* **48,** 2179–2194.

——, ——, and ——, 1993: Frontal dynamics near and following frontal collapse. *J. Atmos. Sci.,* **50,** 3194–3212.

Uccellini, L. W., and S. E. Koch, 1987: The synoptic setting and possible energy sources for mesoscale wave disturbances. *Mon. Wea. Rev.,* **115,** 721–729.

Van Tuyl, A. H., and J. A. Young, 1982: Numerical simulation of nonlinear jet streak adjustment. *Mon. Wea. Rev.,* **110,** 2038–2054.

Vanneste, J., and I. Yavneh, 2004: Exponentially small inertia–gravity waves and the breakdown of geostrophic balance. *J. Atmos. Sci.,* **61,** 211–223.

Zhang, F., 2004: Generation of mesoscale gravity waves in upper-tropospheric jet–front systems. *J. Atmos. Sci.,* **61,** 440–457.